Electronic Supporting Information

Scalable one-step production of electrochemically exfoliated graphene decorated with transition metal oxides for high-performance supercapacitors

Adrian Romani Vazquez[a], Christof Neumann[b], Mino Borrelli[a], Huanhuan Shi[a], Matthias Kluge[c], Wajdi Abdel-Haq[d], Martin R. Lohe[a,e], Carsten Gröber[f], Andreas Röpert[f], Andrey Turchanin[b], Sheng Yang*[a], Ali Shaygan Nia*[a] and Xinliang Feng*[a]

*: Corresponding authors
[a] Center for Advancing Electronics Dresden (CFAED) & Chair of Molecular Functional Materials, Faculty of Chemistry and Food Chemistry, Technische Universität Dresden, Helmholtzstraße 10, 01069, Dresden, Germany
E-mail: s.yang@fkf.mpg.de, ali.shaygan_nia@tu-dresden.de, xinliang.feng@tu-dresden.de
[d] Institute of Physical Chemistry, Abbe Center of Photonics, Center for Energy and Environmental Chemistry (CEEC) at Friedrich Schiller University, Lessingstr. 10, Jena, 07743 Germany
[c] Chair of Macromolecular Chemistry, Faculty of Chemistry and Food Chemistry, Technische Universität Dresden, Helmholtzstraße 10, 01069, Dresden, Germany
[d] Max Planck Institute for Chemical Physics of Solids, 01187 Dresden, Germany
[e] Sixonia Tech GmbH, Maria-Reiche-Str. 3, D-01109 Dresden, Germany
[f] Interactive Wear AG, Petersbrunner Str. 3, D-82319 Starnberg, Germany

Contents

1. Development and Characterization of TMO-EG materials

In this section, we provide additional data and insights into the TMO-EG materials developed, as shown in the main text.

Regarding Scanning Electron Microscopy (SEM), the in-lens detector with the high spatial resolution was used to assess the morphology differences between the control samples (EG, **Figure 2E**) and graphene exfoliated in the presence of metal salts (**Figure 2 F-G**, **Figures S2, S3, S5, S7, S9, S10**). Moreover, as the metal atoms are significantly heavier than carbon or oxygen, a backscatter detector (ESB) was also used to confirm the successful decorations by heavy metals.

1.1.Non-functionalized graphene (EG)

EG was produced and characterized as a control sample to evaluate the impact of the *in-situ* functionalization and decoration of the flakes.

The XPS analysis of the C 1s peak of EG (**Figure S1 A-C**) showed that 76.9% of the carbon corresponds to sp^2-carbon, similar to previous reports on the electrochemical exfoliation[1].

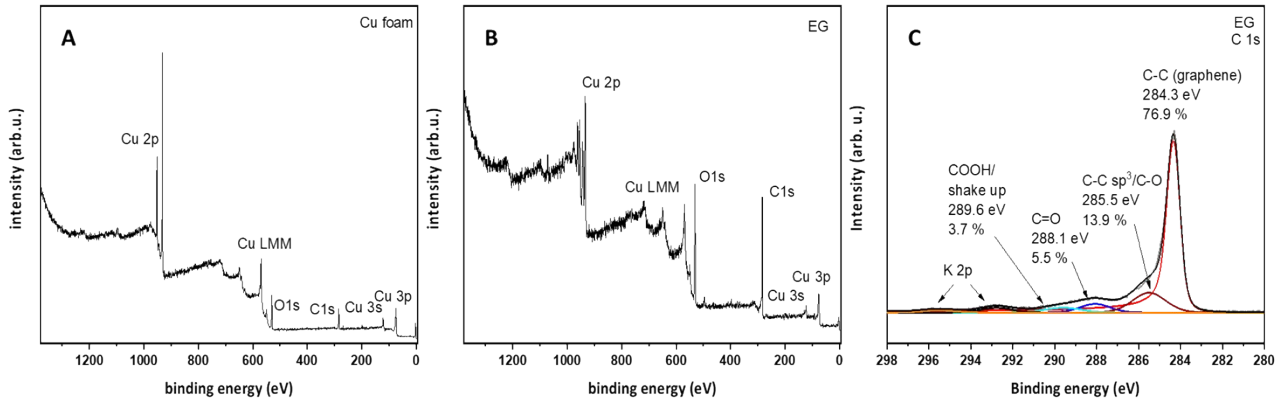

Figure S1. XPS overview spectrum of of copper foam blank (A), EG control (B) as well as high-resolution C 1s spectrum of EG (C)

1.2.CoO_x-EG

The TGA showed (**Figure 2 A**) that cobalt did not decorate the surface of the graphene flakes. The XPS spectrum further confirmed the unsuccessful decoration (**Figure S2**), where Co 2p peak showed only noises, and C1s signal showed similar features to the EG sample. However, the amount of sp^2-bonded graphene was slightly higher than EG (80% vs. 76.9%) (**Figure S2 B**), which could be related to the protection of EG flakes by Co salts[2]. SEM images (**Figure S2 C-E**) also showed undecorated flakes.

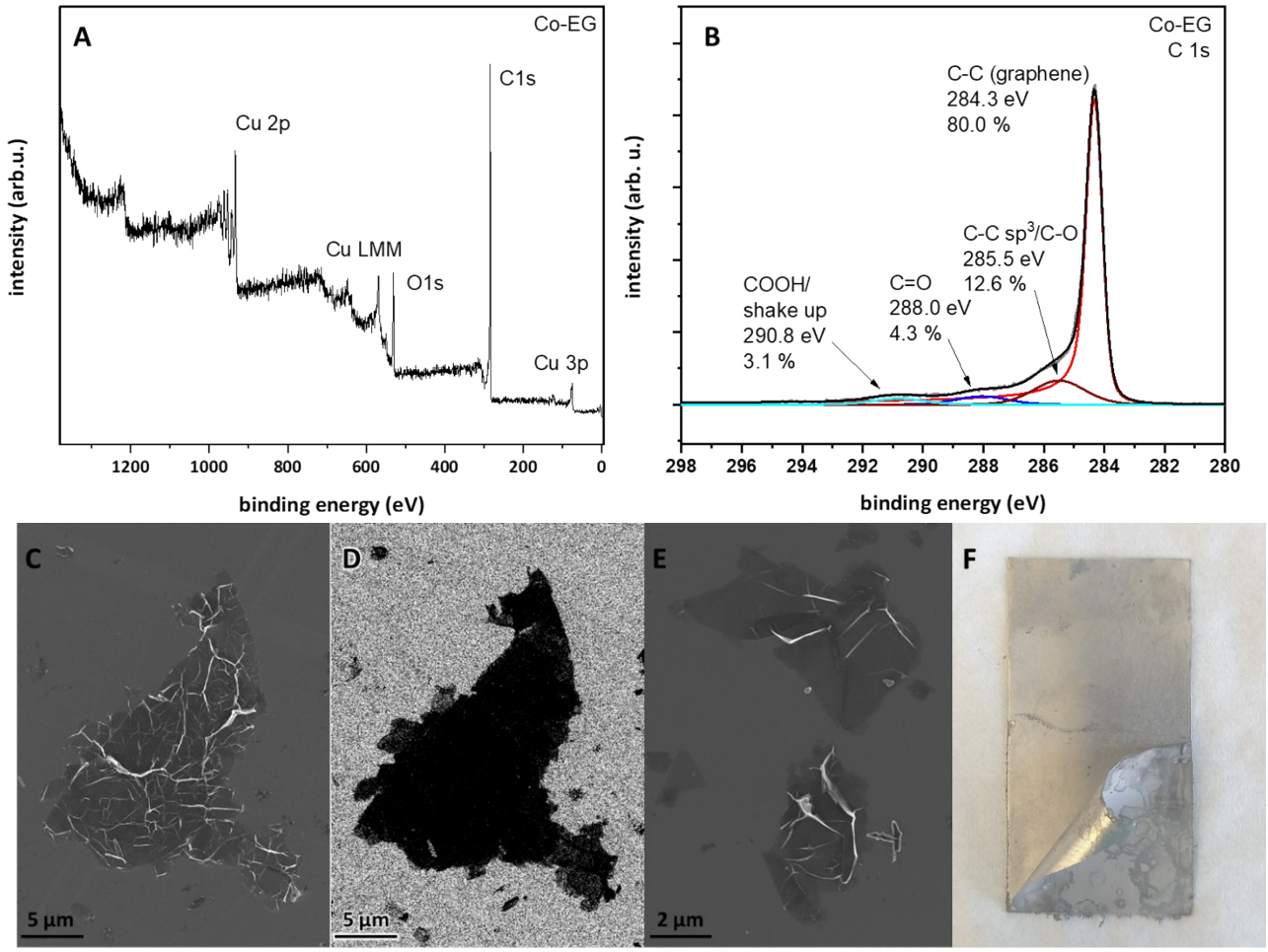

Figure S2. XPS overview spectrum of CoO_x-EG (A) and high-resolution C 1s spectrum (B). SEM micrograph of large undecorated flake exfoliated in the presence of $CoSO_4$ (C). Note the lack of backscatter response indicating that no heavy elements are on the graphene (D). Additional example of undecorated flakes (E). Co-based film on titanium cathode formed during exfoliation (F).

1.3.NiO_x-EG

EG exfoliated in the presence of nickel sulfate showed very similar results to CoO_x-EG in the XPS (**Figure S3**), with minimal trace amounts of Ni (≈0.1 at%) and a noticeably higher sp^2-bonded carbon percentage than EG (83.2% vs 76.9%). Additionally, SEM images showed undecorated EG flakes (**Figure S3 C**).

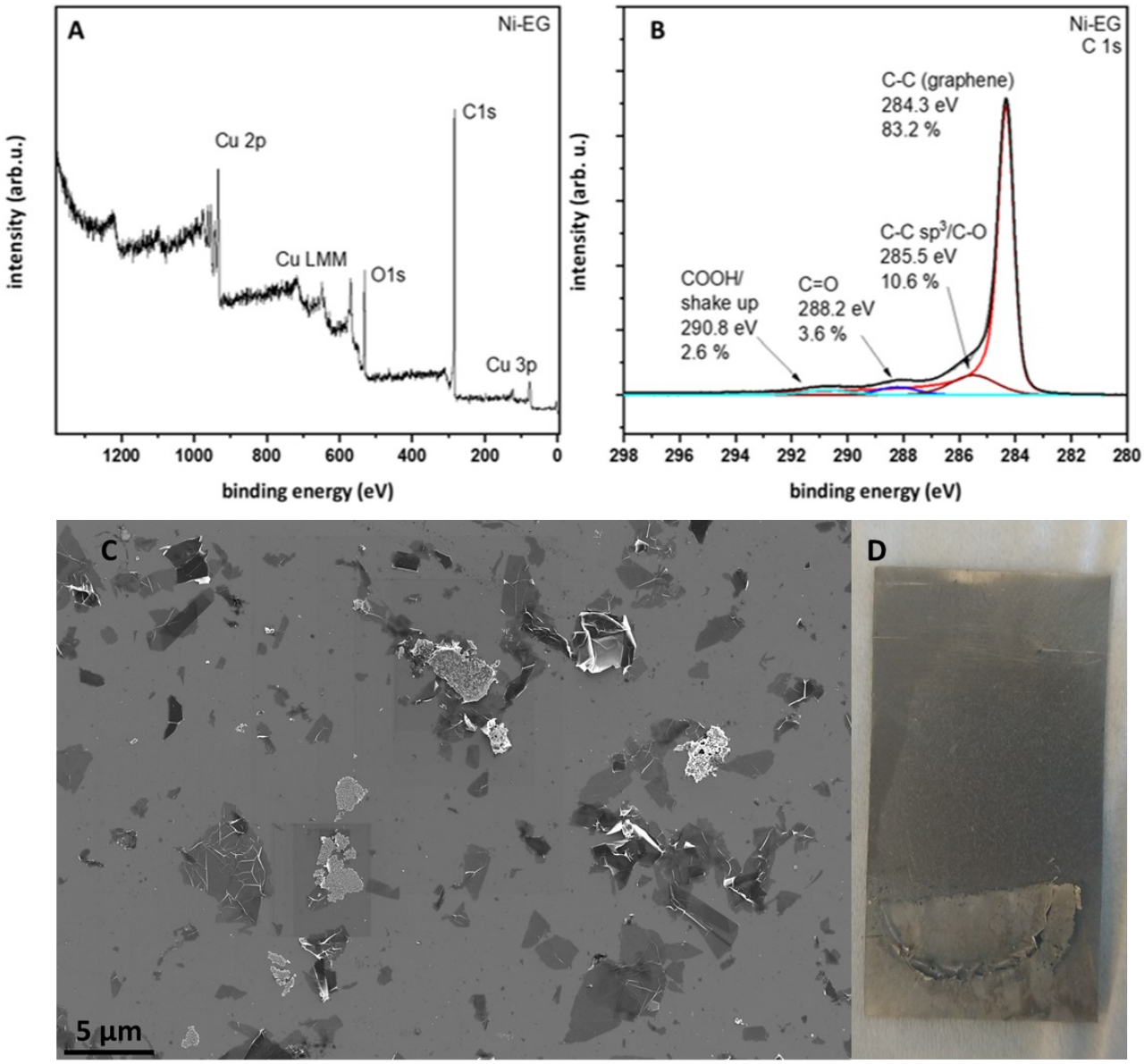

Figure S3. XPS overview spectrum of NiO_x-EG (A) and high-resolution C 1s (B). Wide-field SEM image showing undecorated flakes and debris from the nickel source (C). Ni-based film on titanium cathode after exfoliation (D).

1.4.VO_x-EG

For this sample, the XPS spectrum showed both an increase in the sp^2 bond percentage of carbon from 76.9% to 84.2% **(Figure S4 B)** and low amounts (0.2 at%) of oxidized vanadium (**Figure S4 C**). While the data fits a high oxidation state for the metal, it is not possible to precisely determine whether the metal is V(IV) or V(V) due to the low signal-to-noise ratio (SNR). Moreover, both oxidation states have very similar binding energies in the range of 516.5 - 517 eV[3]. Additionally, SEM images showed the presence of vanadium oxide particles on EG flakes (**Figure S5**).

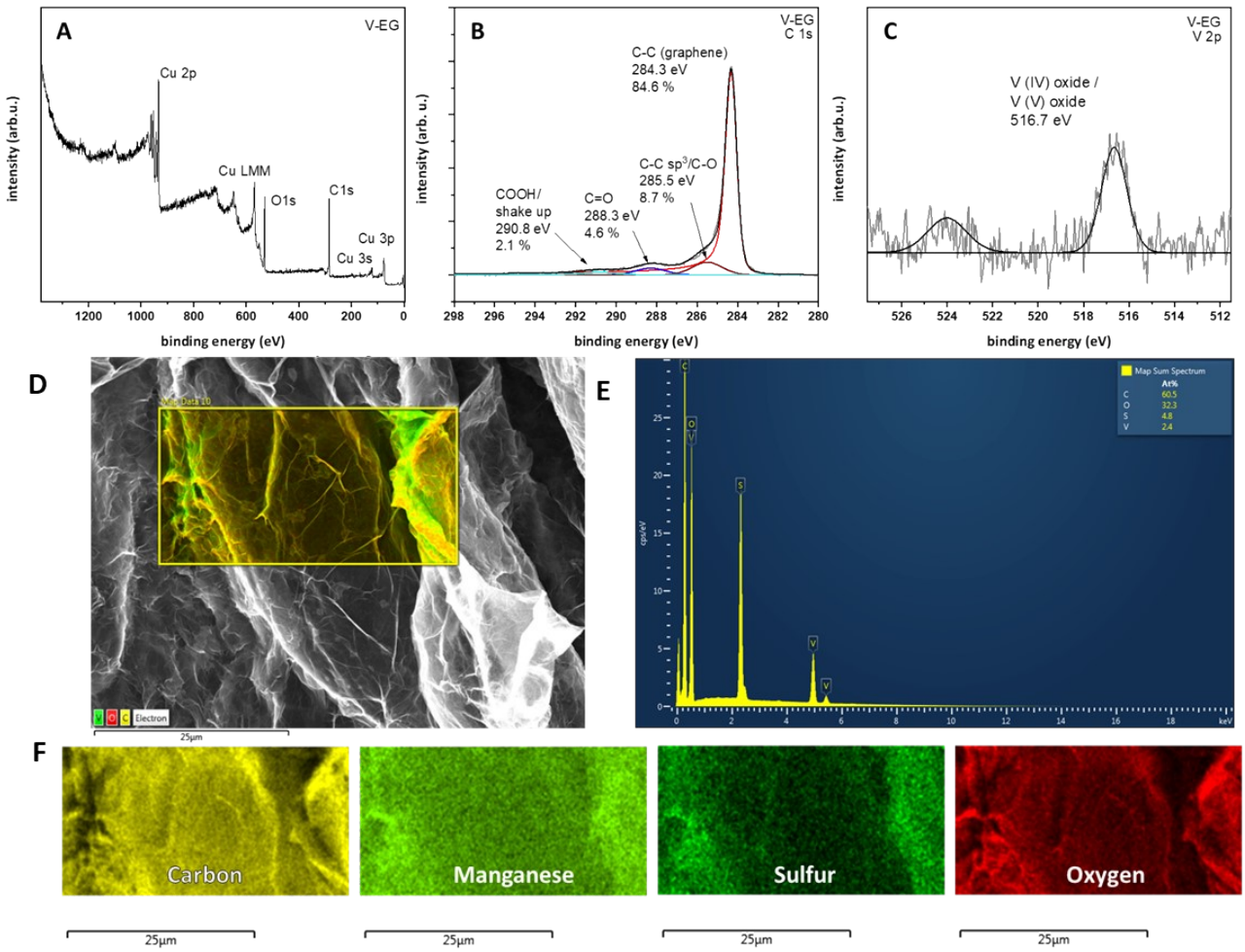

Figure S4. XPS overview spectrum of V-EG (A), high-resolution C 1s spectrum (B) and high-resolution V 2p spectrum (C). SEM/EDS layered image (D), EDX spectrum (E) and elemental maps (F) of graphite anode after 1 minute of intercalation.

The electrochemical performance of VO_x-EG (**Figure 3 A**) showed a significantly improved capacitance compared to EG, further confirming the successful decoration of EG flakes by VOx.

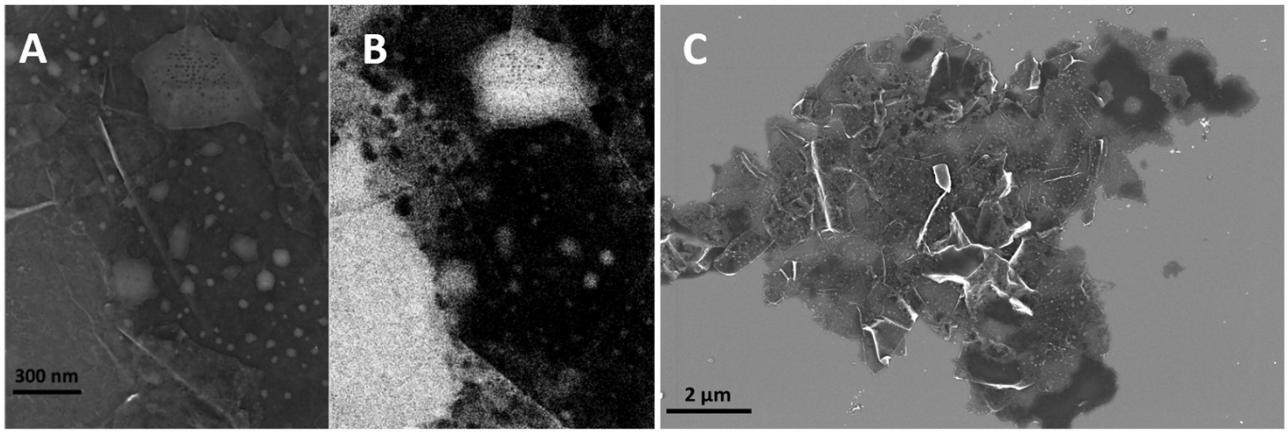

Figure S5. A) Close-up detail of VO_x-EG flakes. B) ESB image of the same VO_x-EG flake. C) Large VO_x-EG flake showing extent of decoration on the surface.

1.5.FeO_x-EG

In the case of FeO_x-EG, a higher signal from iron was detected in the 730-710 eV range, corresponding to 0.8 at% FeOx loading, although the quantification was difficult due to the nearby presence of Cu Auger bands. On the other hand, the protective effect of $FeSO_4$ on the structure was less pronounced, with a minimal increase of the sp^2-bonded carbon from 76.9% to 78.5% (**Figure S6 B**). Analysis of the iron's oxidation state was done *via* background subtraction and fitting of the Fe 2p peak[4,5] (**Figure S6 C**). Unfortunately, while it is clear that iron is oxidized as metallic Fe would peak at 707-708 eV, it is not possible to determine the exact oxidation state in this sample due to this complex Cu background. EDX analysis of the graphite anode also confirmed the diffuse presence of Fe at the beginning of the exfoliation process **(Figure S6)**.

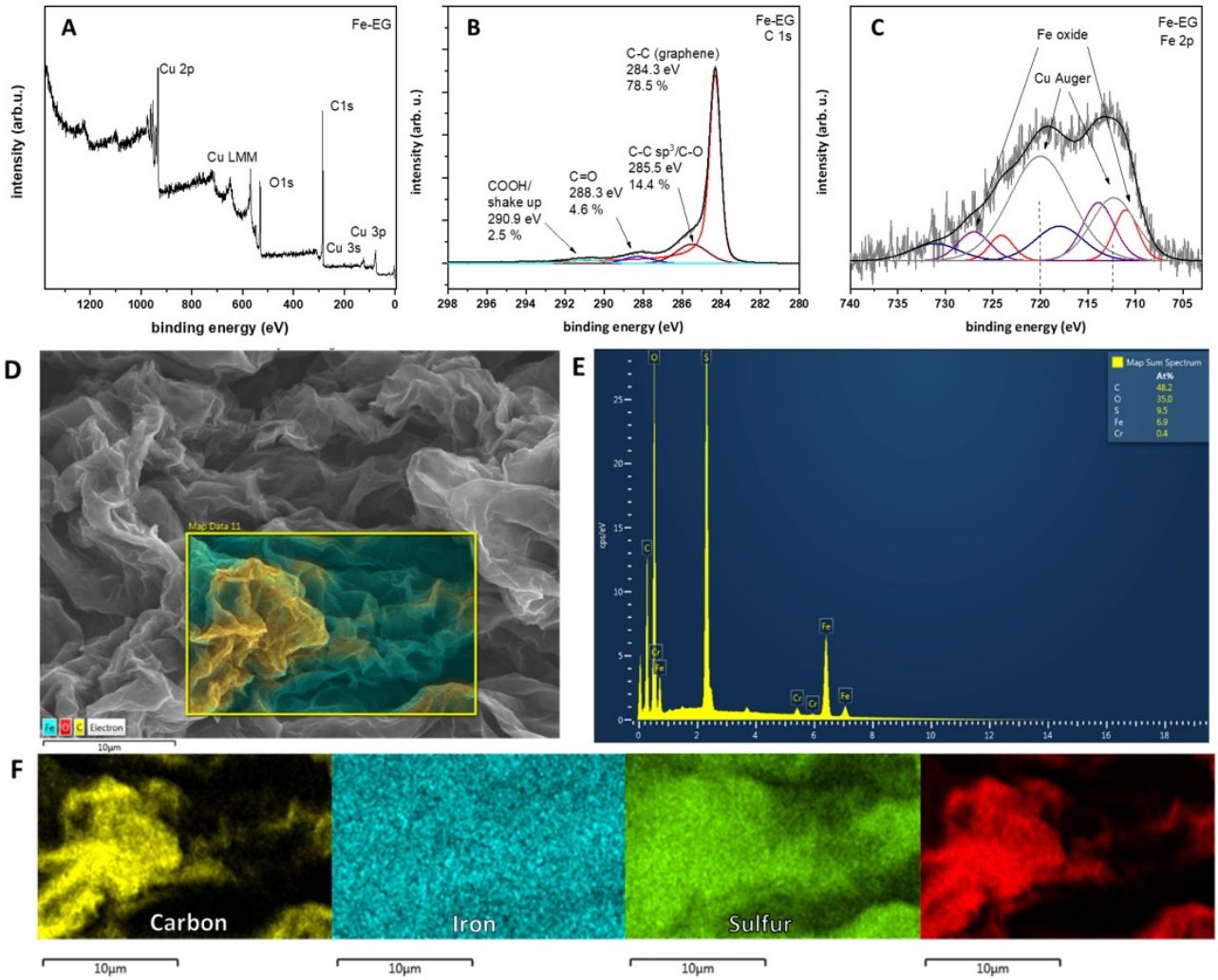

Figure S6. XP overview spectrum of FeO_x-EG (A), high-resolution C 1s spectrum (B), and high-resolution Fe 2p spectrum (C). SEM/EDS layered image (D), EDX spectrum (E), and elemental maps (F) of graphite anode after 1 minute of intercalation.

Like VO_x-EG, electrochemical testing showed FeO_x-EG to have a capacitance of 65 F/g as a negative electrode. Moreover, SEM showed flakes with different loading, including undecorated, heavily decorated, and partially decorated **(Figure S7**).

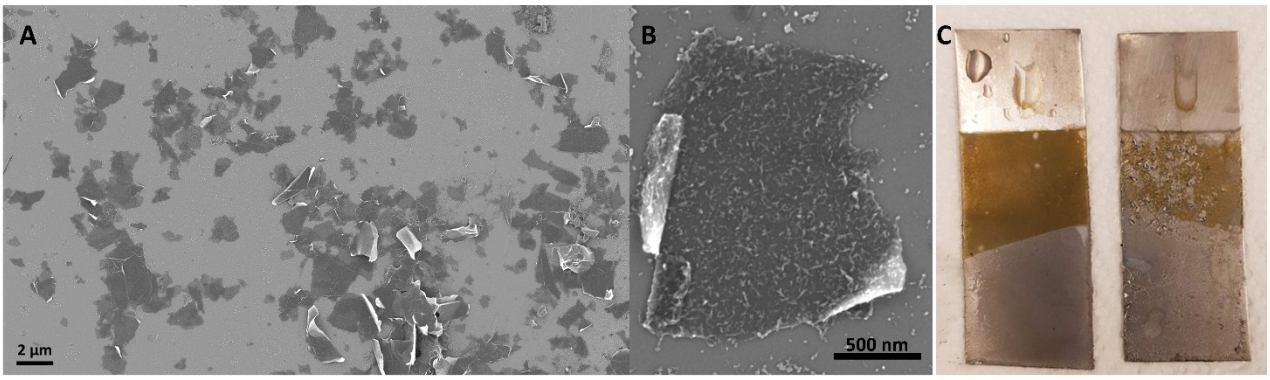

Figure S7. Wide-field image of FeO_x-EG showing both undecorated and decorated flakes (A) and detail of a decorated Fe-EG flake (B). Cathodic deposition of Fe-based film after 1 minute of exfoliation process (C).

1.6.TiO_x-EG

For this material, a 2.4 at% of Ti was detected. Moreover, the sp^2 carbon amount was also high at 82.2% (**Figure S8-B**), indicating an excellent protective effect on the graphene. Analysis of the Ti 2p peak shows a doublet, indicating that Ti is oxidized. The spectrum fits well to Ti (IV)[3], corresponding to TiO_2 (**Figure S8-C**). The EDX analysis after 1 minute of intercalation again proved the near-instantaneous apparition of Ti on the graphite cathode (**Figure S8 D-F**).

The decoration of EG flakes was also confirmed by SEM (**Figure S9**), although due to the poor dispersibility of TiO_x-EG in different solvents, including DMF, most of the flakes reaggregated during sample preparation.

Finally, the higher loading of TiO_2-EG achieved the second-highest capacitance of the samples tested (**Figure 3A**), with values of 63 and 76 F/g as the positive and negative electrodes, respectively.

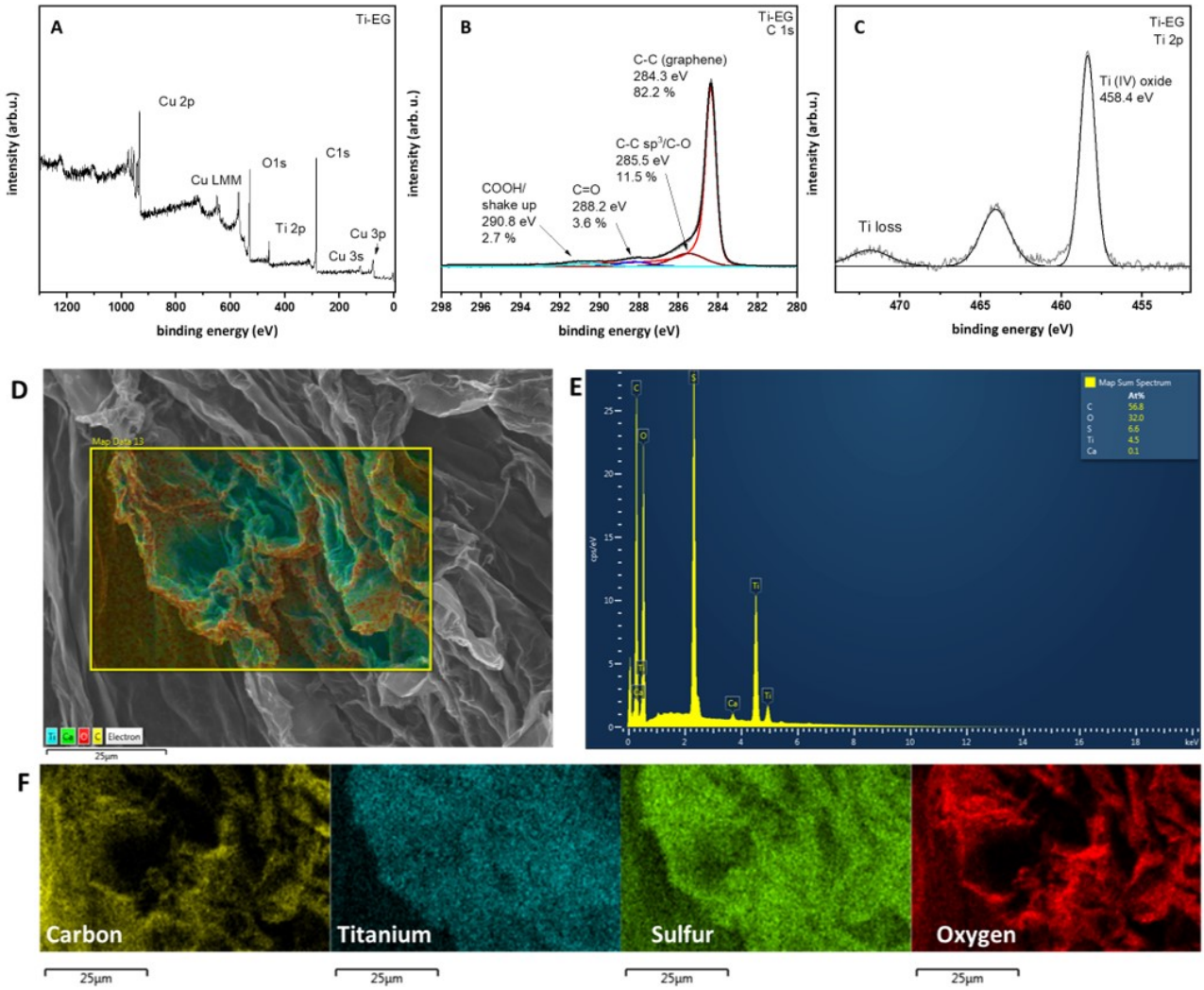

Figure S8. XP overview spectrum of TiO_x-EG (A), high-resolution C 1s (B) and high-resolution Ti 2p spectrum (C). SEM/EDS layered image (D), EDX spectrum (E) and elemental maps (F) of graphite anode after 1 minute of intercalation.

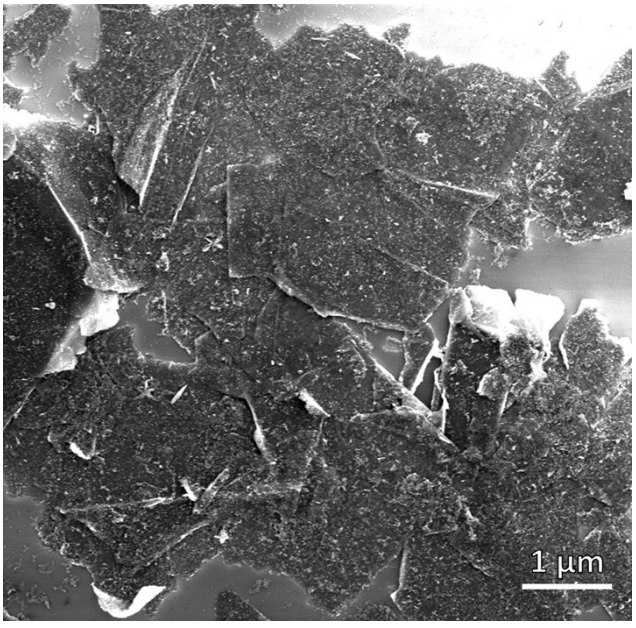

Figure S9. SEM image of TiO_x-EG flakes

1.7.Additional characterization of MnO_x-EG

The flower-like growths on the basal plane of the graphene flakes show a morphology similar to previous reports of MnO_x decorations[6] (**Figure S10 A&B**). In particular, in MnO_x-EG, a small proportion of the growths were present in the layered structures, with the MnO_x sandwiched between graphene layers (**Figure S10 C&D**) where the attenuated signal from these decorations was more noticeable under the in-lens image, while the ESB image accurately picked up the signal from the heavier elements. Additional STEM imaging showed more flakes with varying degrees of decoration **(Figure S10 E-H**); two clearly distinct types of deposition are visible, one dot-like and one flower-like. We propose that the crystalline needles correspond to MnO_2, while the dot-type decorations are related to the Mn_2O_3 and its complexation being less crystalline; this fits well with XPS and XRD results (**Figure 2 B-E**). The STEM imaging was obtained from MnO_x-EG produced in the continuous flow reactor, showing the similarity in morphology for both beaker-type and continuous flow exfoliations.

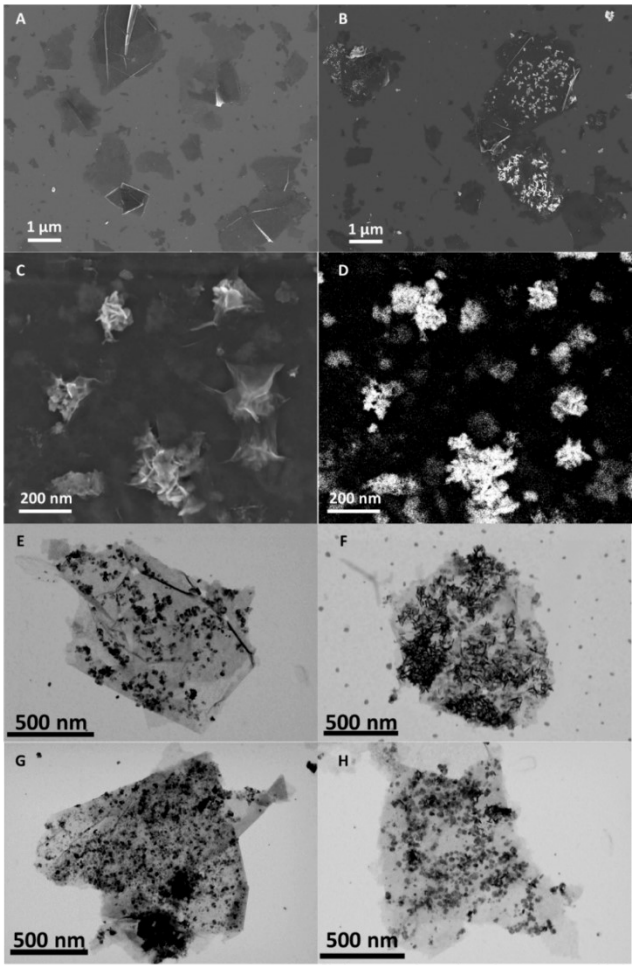

Figure S10. SEM micrographs of non-functionalized EG flakes (A) and MnO_x-EG (B) hybrid flakes, showing decorations on the basal plane. SEM detail of Mn decorations on graphene flake using in-lens detector (C) and ESB image of the same flake (D). STEM images of different MnO_x-EG flakes (E-H) produced in the continuous flow reactor.

The Pourbaix diagram (**Figure S11 A**) indicates the stable species of Mn in aqueous media at different pH and potential values. Additionally, to prove that both the exfoliation of graphene and its functionalization with TMO happen simultaneously, the intercalated graphite electrode was analyzed via SEM/EDX (**Figure S11 B-G**) after one minute of exfoliation, showing that both manganese and sulfate are present in between graphite layers. **Figure S11 H** shows the rapid color change of the electrolyte after the application of voltage, indicating the oxidation of Mn.

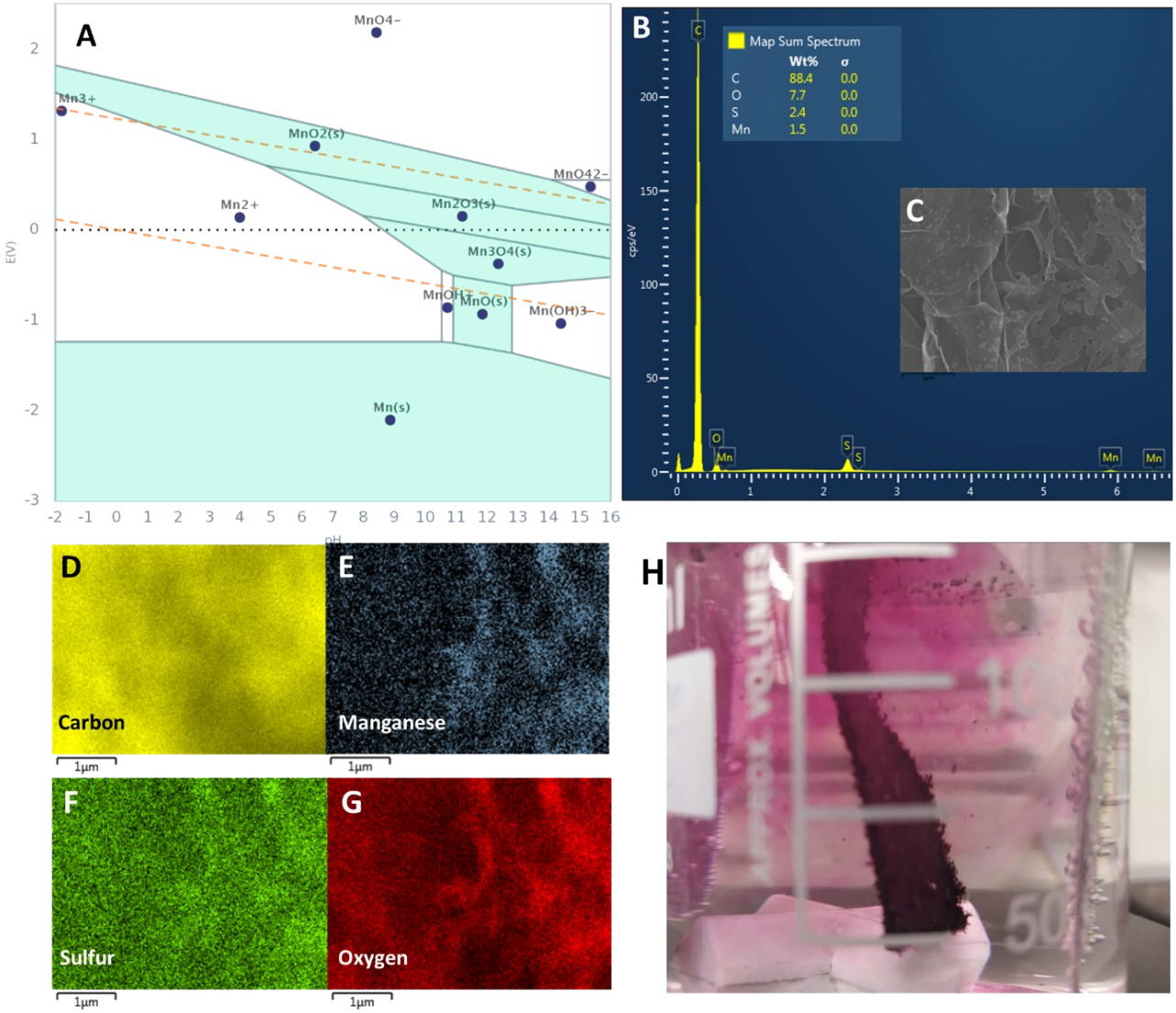

Figure S11. Pourbaix diagram of Mn (A). EDX spectrum (B) of graphite foil electrode after 1 minute of intercalation with $H_2SO_4/MnSO_4$ electrolyte with SEM image of the measured area (C) and elemental maps (D-G). Digital photograph of the same graphite anode after 5 seconds of the intercalation process, showing the electrolyte color change (H).

2. Electrode characterization of MnO_x-EG and comparison between Mn sources

All the *in-situ* functionalized samples showed significantly improved capacitance compared to EG (**Figure 3**), proving that the presence of TMO_x is the main source of electrochemical performance. Manganese-based material has been shown to display a competitive theoretical performance in recent works[7,8], and has been compared by Zhi et al.[9] with other metals. For example, the capacitance of MnO_2 was measured as 1380 F/g[10], even better than RuO_2 (1340 F/g)[11] and only 10% lower than Co_3O_4 (1525 F/g in device). Comparing the capacitance of the developed MnOx-EG hybrid (23 wt% loading) with the theoretical values of manganese oxides[12] would show efficiency of ~75%. The discrepancy could be explained by accessibility issues; as seen in the SEM micrographs (**Figure S10 C-D**), manganese can be present in multi-layered structures, which would reduce the contact of the MnO_x decorations with the electrolyte.

Once MnO_x-EG was determined to be the most promising candidate material, we set out to optimize its production. To do so, we tested different concentrations of Mn sources in the electrolyte. Higher concentrations were tested to explore the upper decoration limits. Additionally, manganese acetate (MA series) instead of manganese sulfate (MS series) was also tested to evaluate the importance of the chosen salt. The results in **Figure S12 B** show that the capacitance improved only slightly above 30 mM of Mn salt. The evaluation of the MA series and the cycling stability of all samples is also displayed in **Figure S11**. Here it can be seen that the CV curves (**Figure S11 A&C**) have a very similar shape regardless of salt source. Moreover, while capacitance is comparable between sources (**Figure S11 B&D**), cycling stability was improved when sulfate salt was employed (**Figure S11 E**). We have also been able to draw a correlation between the TGA residue **(Figure S11 F)** and the capacitance of the sample **(Figure S13**), which further proves MnO_x as the main contributor to capacitance due to its strong pseudocapacitive behavior.

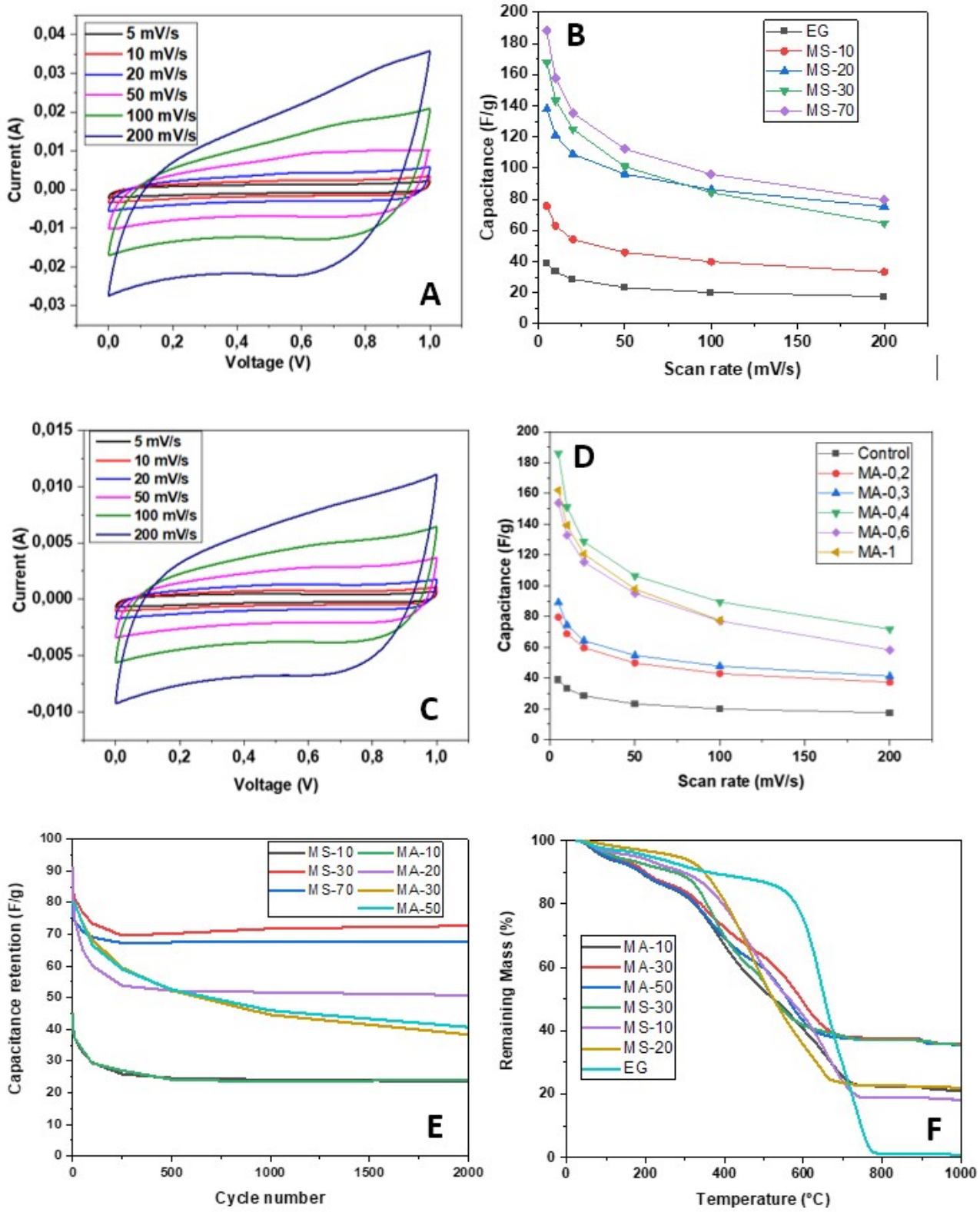

Figure S12. CV of MS-30 (A) and gravimetric capacitance of MS samples, with a physical mixture of 20% MnO_2 and 80% non-functionalized EG as control (B). CV of MnO_x-EG using 30 mM manganese acetate (MA) as metal source and capacitance of MA-EG samples (D). Comparison of cycling stability at 100 mV/s between MS and MA samples, with MS demonstrating much higher capacitance retention (E). TGA of different MnO_x-EG materials showing the loading limit to be similar regardless of source (F).

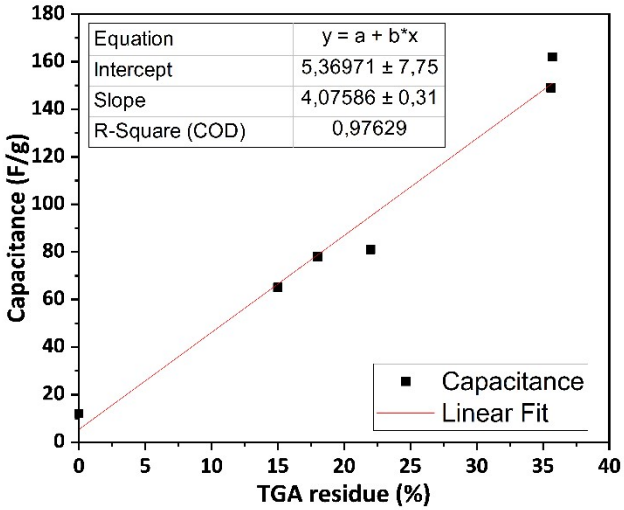

Figure S13. Relationship between TGA residue and capacitance of different MnO_x-EG hybrids. The point at 0% load is taken from EG.

3. Reactor design and optimization

The most critical requirement during upscaling is reproducibility, ensuring that different reactor sizes behave comparably which would greatly simplify subsequent capacity increases. A single-cell, prism-shaped reactor (**Figure 1 B**) was selected due to its simple geometric modeling and the possibility to construct new reactors.

Initially, we hypothesized that the production rate and, critically, the quality of electrochemically exfoliated graphene (EG) depends on the geometry of the reactor. Therefore, a reactor capable of working with different geometric configurations was designed and constructed (**Figure 1**). Additional views and parameters are displayed in **Figure S14**. In this design, the slits on the electrodes can be used to adjust both distance (up to 4 cm from cathode to anode) and height (up to 5 cm of immersed foil), allowing for detailed geometry studies.

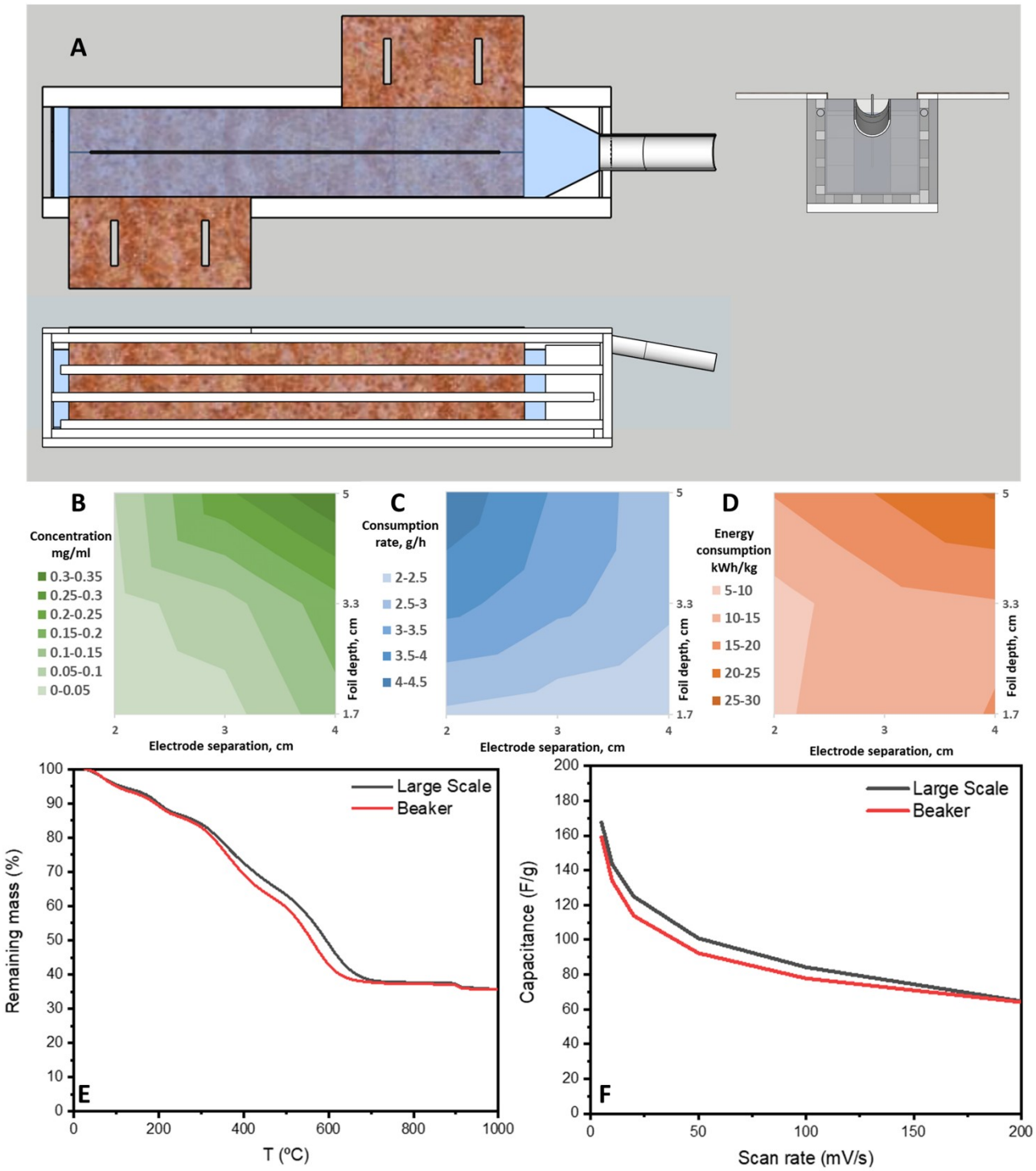

Figure S14. Additional reactor projections, with side plate removed for visibility (A). Response surfaces for EG dispersibility (B), production rate (C), and energy consumption (D). The TGA under synthetic air (E) and capacitance (F) comparison of Mn-EG from beaker and large-scale reactor show that the material's characteristics and performance are maintained.

Another consideration is that optimization must have a specific target. We have optimized the geometry to maximize the dispersibility of EG, as this is generally the most useful fraction of the product. For an initial assessment, all EG produced for these tests was sonicated in DMF with a bath sonicator for 60 min.

As can be seen in the surface response graphs (**Figure S14 B-D**), the best result for concentration was achieved with 5 cm depth and 10 cm electrode separation showing that the maximum foil consumption rate does not lead to the best quality of EG. This could be related to longer exfoliation times needed for efficient intercalation and decoration.

As mentioned in the main text, we found that lengthening the graphite foils does not affect dispersibility (with values of 0.35±0.02 mg/ml for foils between 10 and 45 cm long). Therefore, we propose that the cross-section of the reactor, as shown in **Figure S15**, offers a good model of the electrochemical exfoliation of graphite in this type of reactor.

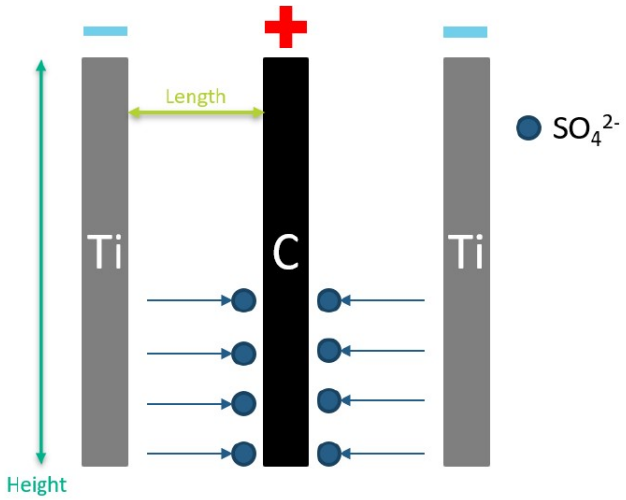

Figure S15. Cross-section model of exfoliation reaction.

4. Supercapacitor device testing

Additional characterization is shown in **Figure S16**. Note that the CV curves at cycles 2000-6000 of galvanostatic charge-discharge are almost identical, showing a 96% capacitance retention over the 4000-cycle period. This gives a good indication of the long-term stability of the material.

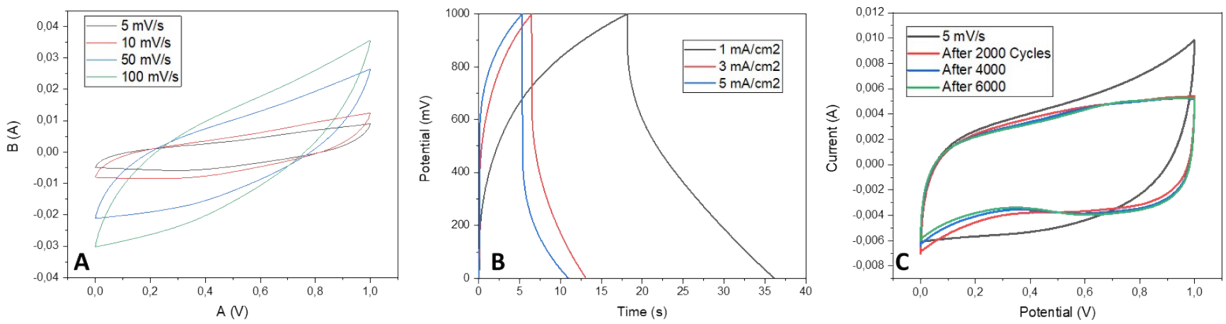

Figure S16. electrochemical tests of supercapacitor device. A: CV curve at different scan rates. B: Chronopotentiometry. C: CV curve at 5 mV s^{-1} after 2000-6000 cycles of charge/discharge.

Moreover, **Tables S1** and **S2** compare our work with similar materials and devices in recent literature.

5. Additional electrochemical characterization of other TMO-EGs

Figure S17 shows the 5 mV s^{-1} voltammograms of the other TMO-EGs.

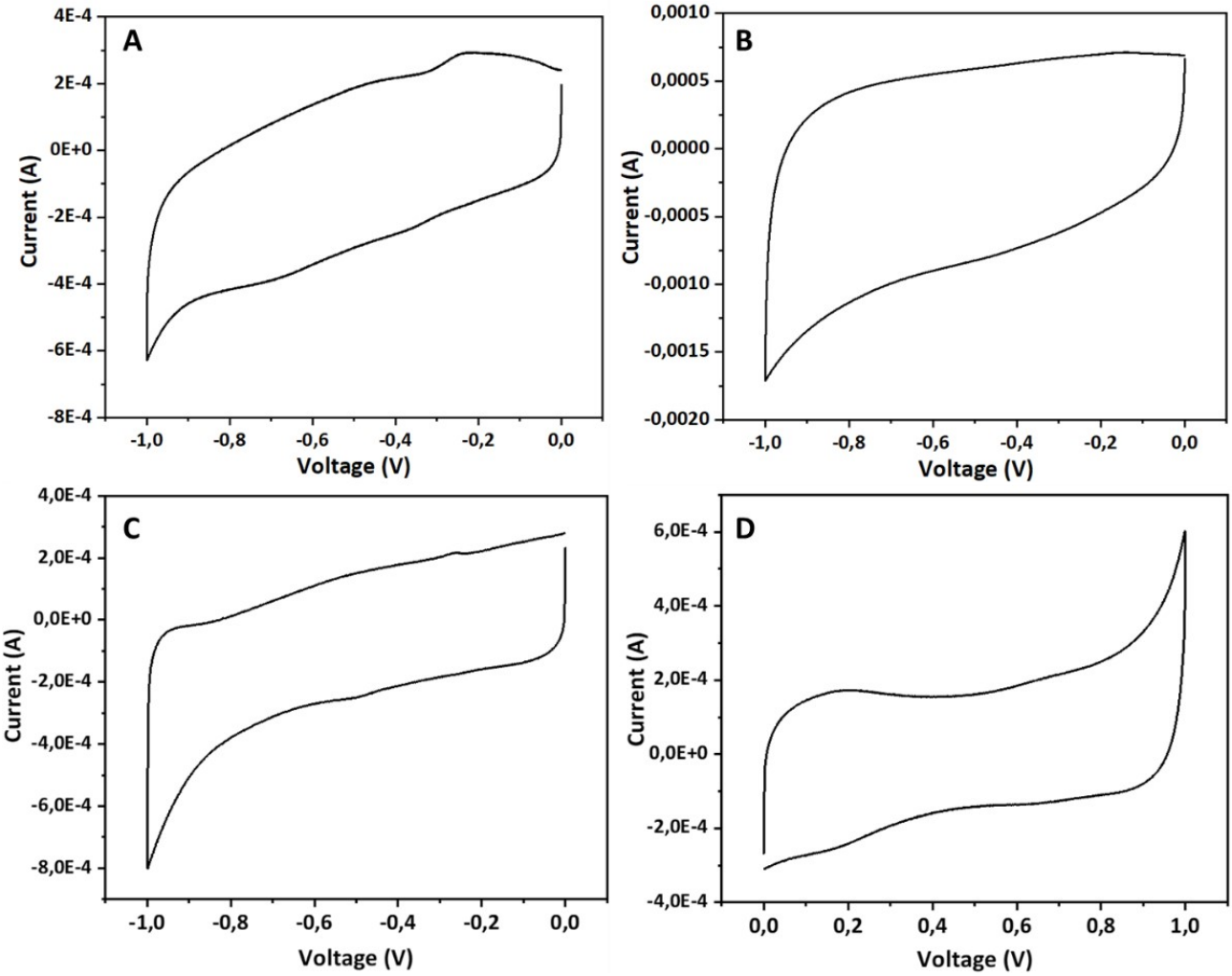

Figure S17. CV at 5 mV s^{-1} of FeO_x-EG (A), VO_x-EG (B), and TiO_x-EG (C, D).

Table S1. Comparison of electrodes with relevant works

Sample	SC (F/g)	Production method	Electrolyte	V Window	Reference
MnO_x-EG (MS-30)	170 @ 5 mV/s (1.6 A/g)	Electrochemical exfoliation	4M LiCl	0-1	This work
G-Mn_3O_4-RuO_2	407 @ 2 mV/s	Electrochemical exfoliation	6M KOH	0-2	[2]
3D-Porous N-doped Graphene	405 @ 1 A/g	PET + Urea @ 800 ºC	6M KOH	0-1.1	[13]
Co_2AlO_4+MnO_2	915 @ 2 A/g	Hydrothermal growth on Ni foam	2M KOH	0-0.4	[14]
V_2O_5 NS-rGO	635 @ 1 A/g	Hydrothermal synthesis V2O5 + Hummers for GO	1M KCl	0-0.8	[15]
Metalorganic Quantum Dots	51.7 @ 0.5 A/g	Heat/Acid treatment	1M $LiPF_6$	2-4	[16]

Table S2. Device comparison

Sample	SC (F/g)	Cap. (mF/cm2)	ED (Wh/kg)	PD (W/kg)	Production method	Device fabrication	V Window	Reference
MnO_x-EG (MS-30)	170	52	20.8	6000	Electrochemical exfoliation	Screen printed supercapacitor	0-1	This work
G-Mn_3O_4-RuO_2 on Ionic Liquid	287		-	-	Electrochemical exfoliation	Coin cell	0-2	[2]
3D-Porous N-doped Graphene	405		68.1	559	PET + Urea @ 800 ºC	2-electrode cell	0-1.1	[13]
$Ni(OH)_2$/Carbon Nanosheets	198		56.7	4000	Resin growth + ion exchange	2-electrode cell	0-1.6	[17]
Co_2AlO_4+MnO_2 // Fe_3O_4	99.1		35.3	8033	Hydrothermal growth on Ni foam	Asymmetric sandwich structure	0-1.6	[14]
V_2O_5 NS // rGO	124		75.9	30000	Hydrothermal synthesis V2O5 + Hummers for GO	Asymmetric sandwich structure	0-1.6	[15]
SnO2/rGO/Ni	-	109	11.8 μWh cm^{-2}	14.2 mW cm^{-2}	Chemical post-functionalization of rGO + Ni sputtering on SnO2/rGO film	2-electrode cell	0-1.8	[18]
F-modified graphene	-	17.4	56 mWh cm^{-3}	21 W cm^{-3}	Electrochemical exfoliation	Microsupercapacitor	0-3.5	[19]

6. Bibliography

1 S. Yang, M. R. Lohe, K. Müllen and X. Feng, *Adv. Mater.*, 2016, **28**, 6213–6221.

2 A. Ejigu, K. Fujisawa, B. F. Spencer, B. Wang, M. Terrones, I. A. Kinloch and R. A. W. Dryfe, *Adv. Funct. Mater.*, 2018, **28**, 1804357.

3 A. V. Naukin, A. Kraut-Vass, S. W. Gaarenstroom and C. J. Powell, *NIST Stand. Ref. Database Number 20*, , DOI:dx.doi.org/10.18434/T4T88K.

4 H. Lv, H. Zhao, T. Cao, L. Qian, Y. Wang and G. Zhao, *J. Mol. Catal. A Chem.*, 2015, **400**, 81–89.

5 M. C. Biesinger, B. P. Payne, A. P. Grosvenor, L. W. M. Lau, A. R. Gerson and R. S. C. Smart, *Appl. Surf. Sci.*, 2011, **257**, 2717–2730.

6 X. Lv, H. Zhang, F. Wang, Z. Hu, Y. Zhang, L. Zhang, R. Xie and J. Ji, *CrystEngComm*, 2018, **20**, 1690–1697.

7 A. Huang, W. Zhou, A. Wang, M. Chen, Q. Tian and J. Chen, *J. Energy Chem.*, 2021, **54**, 475–481.

8 A. Khan, H. Wang, Y. Liu, A. Jawad, J. Ifthikar, Z. Liao, T. Wang and Z. Chen, *J. Mater. Chem. A*, 2018, **6**, 1590–1600.

9 M. Zhi, C. Xiang, J. Li, M. Li and N. Wu, *Nanoscale*, 2013, **5**, 72–88.

10 M. Toupin, T. Brousse and D. Bélanger, *Chem. Mater.*, 2004, **16**, 3184–3190.

11 C.-C. Hu, W.-C. Chen and K.-H. Chang, *J. Electrochem. Soc.*, 2004, **151**, A281.

12 S. Ji, Y. Ma, H. Wang, J. Key, D. J. L. Brett and R. Wang, *Electrochim. Acta*, 2016, **219**, 540–546.

13 N. A. Elessawy, J. El Nady, W. Wazeer and A. B. Kashyout, *Sci. Rep.*, 2019, **9**, 1129.

14 F. Li, H. Chen, X. Y. Liu, S. J. Zhu, J. Q. Jia, C. H. Xu, F. Dong, Z. Q. Wen and Y. X. Zhang, *J. Mater. Chem. A*, 2016, **4**, 2096–2104.

15 D. H. Nagaraju, Q. Wang, P. Beaujuge and H. N. Alshareef, *J. Mater. Chem. A*, 2014, **2**, 17146–17152.

16 G. Li, Z. Yin, H. Guo, Z. Wang, G. Yan, Z. Yang, Y. Liu, X. Ji and J. Wang, *Adv. Energy Mater.*, 2019, **9**, 1802878.

17 M. Xie, Z. Xu, S. Duan, Z. Tian, Y. Zhang, K. Xiang, M. Lin, X. Guo and W. Ding, *Nano Res.*, 2018, **11**, 216–224.

18 S. Byun, B. Shin and J. Yu, *Carbon N. Y.*, 2018, **129**, 1–7.

19 F. Zhou, H. Huang, C. Xiao, S. Zheng, X. Shi, J. Qin, Q. Fu, X. Bao, X. Feng, K. Müllen and Z. Wu, *J. Am. Chem. Soc.*, 2018, **140**, 8198–8205.